ELSEVIER

Contents lists available at ScienceDirect

# Chemical Engineering Journal

journal homepage: www.elsevier.com/locate/cej





# Deciphering the effect of nucleation/growth kinetics on the morphology of Li plating/stripping on vertically aligned carbon nanofibers - A low-tortuosity 3-D nanostructured carbon host

Sabari Rajendran, Archana Sekar, Jun Li

Department of Chemistry, Kansas State University, Manhattan, KS 66506, United States

# ARTICLE INFO

# Keywords: Lithium metal anode 3-D conductive host Microscopic morphology Nucleation-growth theory Vertically aligned carbon nanofibers

# ABSTRACT

Reversible lithium metal anodes (LMAs) are the holy grail for future rechargeable lithium metal batteries. Threedimensional (3-D) conductive hosts have been extensively explored as an effective approach to suppressing dendrite formation and enabling reversible Li plating/stripping. However, the microscopic morphologies of Li plating and their correlation with the cell performance are not clear. Herein we unravel these issues using the vertically aligned carbon nanofiber (VACNF) array as a model 3-D conductive carbon host which has a welldefined vertical low-tortuosity structure allowing observation of the intrinsic Li morphologies infiltrated into the 3-D host. The VACNF array indeed provides much higher stability and reversibility for Li plating/stripping due to its high surface area and lithiophilic properties. We found that Li plating on both VACNF array and planar Cu electrodes follows the classical nucleation and growth model. Though the low plating current density ( $\leq$ 0.10 mA/cm<sup>2</sup>) provides better cycling stability consistent with the Sand's equation, it forms sparse irregular grains stacked with dendrite-like long Li fibers. In contrast, the moderate to high plating current densities (1.0-5.0mA/cm<sup>2</sup>) produce more uniform Li morphologies consisting of smaller micro-columns or micro-spheres. By decoupling the plating and stripping current densities, we unravel that the more uniform micro-columnar Li infiltrated in the VACNF array obtained at the moderate plating current density (~1.0 mA/cm²) indeed exhibits the highest cycling performance. This provides new insights into the relationship between macroscopic electrochemical tests and microscopic Li morphologies, aiding in optimizing the performance of LMAs based on 3-D conductive hosts.

# 1. Introduction

High energy density batteries are essential for achieving the decarbonization goals in the transition to clean energies and for meeting future energy demands [1]. Lithium metal is considered as the holy grail of anode materials for next-generation high-energy-density batteries owing to its highest theoretical charge storage capacity (3860 mAh/g) and the lowest redox potential (-3.04 V vs. the standard hydrogen electrode (SHE)). Lithium metal anode (LMA), when paired up with high Ni-NMC cathodes (>200 mAh/g) or high-capacity cathodes such as sulfur or oxygen, enables the potential development of batteries with energy densities greater than 500 Wh/kg, significantly surpassing the 350 Wh/kg limit of today's lithium-ion batteries (LIBs) [2,3]. Among all possible configurations of rechargeable lithium metal batteries (LMBs), the anode-free LMBs offer the highest possible theoretical energy density

as it does not involve excess lithium, which also lowers the manufacturing cost and improves the safety in operation [4–7]. Since electrodeposition (or plating) of lithium on the current collector is the key process during the charging step, it is critical to develop a deeper understanding on the lithium nucleation and growth on the current collector. The properties of electrodeposited lithium and the LMA performance are found to strongly depend on the nature of current collector, electrolyte, operating conditions, and plating/stripping parameters [8–13].

Among the influential parameters, the applied current density j has been found to be a key variable since it regulates the rate of reduction of  $\operatorname{Li}^+$  ions to Li metal. Several studies on planar copper current collectors have demonstrated that the microscopic morphology strongly depends on the plating current density j [14–18]. In general, the Li nuclei density  $N_n$  increases with the magnitude of j following the classical nucleation

<sup>\*</sup> Corresponding author.

E-mail address: junli@ksu.edu (J. Li).

and growth theory [14–18]. The plated Li tends to form sparsely distributed large irregular Li nuclei when it is deposited at low j but forms densely populated and more uniform Li particles of smaller sizes at high *j*. On the other hand, macroscopic electrochemical studies have indicated that the electrodeposited Li is more reversible and stable at low j, possibly due to the lower concentration gradient and more homogeneous electric field distribution [19-21]. The formation of dendritic Li structures is accelerated when the Li+ ion concentration depletes at the anode surface. The average time that it takes for the dendrites to start growing is represented by the Sand's time  $t_{Sand}$  [22] which increases as the j is reduced. The microscopic and macroscopic studies seem to point the opposite directions in how to reduce Li dendrite growth by regulating the plating current density j. Since dendrite growth during charging or lithium electrodeposition is one of the critical issues limiting the development of LMAs [23-25], it is important to unravel the hidden connections between the seemingly controversial macroscopic and microscopic observations and develop new mitigating strategies.

Several approaches, such as modification of the current collector, electrolyte and operating parameters, have been successfully developed to mitigate dendrite growth and enhance the coulombic efficiency (CE) and cycle life [26]. The use of high-surface-area three-dimensional (3-D) hosts was found to be effective in delaying the dendrite formation, which was attributed to the reduced local current density *j* and the homogenized electric field compared to those on the planar electrodes [27–30]. The lower j apparently increased the Sand's time  $t_{Sand}$  and delayed the onset of dendrite formation. However, this will make the microscopic morphology of the plated Li more heterogeneous, as predicted by the nucleation and growth theory validated on the planar electrodes. It is expected that the 3-D hosts will induce lower nucleation density (i.e., lower surface coverage) and larger grain sizes due to the lower local current density. But the microscopic morphology of Li plating onto the 3-D hosts and how it changes vs. the plating current density *j* have not been well studied so far. This is challenging since most studies on 3-D host materials employed random porous structures, making it difficult to reveal the microscopic structure of the Li infiltrated into the hosts. In fact, even on planar electrodes, two different morphologies of Li have been reported under the similar conditions of electrodeposition, i.e., at  $j \le 0.1$  mA/cm<sup>2</sup> in the standard ether electrolyte (1.0 M lithium bis(trifluoromethanesulfonyl)imide (LiTFSI) in 1,3-dioxolane (DOL) and 1,2-dimethoxyethane (DME) (v/v 1:1) with 1 wt% LiNO<sub>3</sub> additive) [14,31,32]. Pei et al. [14] and Huang et al. [32] observed island-like Li growth while Park et al. [31] observed fibrous Li growth on planar copper electrodes. The island-like Li growth with a low surface area and low porosity is a desired morphology as it can be stripped more efficiently leaving less dead lithium and SEI. In contrast, fibrous Li is more prone to form dead Li due to the higher probability for breaking off the Li fibers during the non-homogeneous stripping [9,33]. In addition, the higher aspect ratio and larger exposed surface area of fibrous Li would increase the electrolyte consumption due to the repeated SEI formation. It is critical to looking into these issues in 3-D hosts in order to develop reliable LMAs.

In this study, we aim to systematically explore the impact of the Li electrodeposition rate on the morphology of resulting Li deposits on a brush-like 3-D host based on vertically aligned carbon nanofibers (VACNFs) grown on Cu foils. VACNFs are N-doped graphitic carbon fibers grown by plasma-enhanced chemical vapor deposition (PECVD) [34]. They have a unique internal structure consisting of conically stacked graphitic cups along the axis (commonly referred to as bamboolike multi-walled carbon nanotubes (MWCNTs)). The side-wall surface of VACNFs is composed of electrochemically active graphitic edges which are spontaneously oxygenated in the air. In our previous studies, we have demonstrated that the VACNF/Cu can serve as an effective 3-D carbon host to enhance the stability and reversibility of LMAs [27,35]. Given its desirable properties such as the high porosity (~80 %), vertically aligned pore structure and the lithiophilic surface, VACNF/Cu

electrode serves as a model 3-D host for this study. Its well-defined vertical structure allows the observation of the microscopic morphology of infiltrated Li at different stages of Li plating and stripping.

We first demonstrate that a higher pressure between the electrode/ separator stack inside the coin-cells tends to induce densely packed Li morphology, as reported in literature [7,9,36-38]. The non-uniform internal pressure distribution and varied pressure among different coin cells may be the cause for discrepancies among literature. By consistently controlling the coin cell with a minimal pressure, we were able to investigate the intrinsic effect of the plating current density on the microscopic morphology of Li metal plated on both planar Cu and 3-D VACNF/Cu electrodes. The 3-D VACNF/Cu electrode clearly showed superior stability and improved reversibility in continuous plating/ stripping cycling tests. Our results unraveled the drastic change in Li morphology vs. the plating current density on both electrodes, following the classical nucleation and growth theory. Though lowering the local plating current density with the VACNF/Cu electrode exhibited enhanced stability in cycling tests, the formation of large irregular Li grains with the long noodle-like morphology poses a concern for dendrite growth and safety in practical LMBs that require much longer cycling lives. To our surprise, electrochemical characterization showed that the stripping current density also affected the electrode performance. By decoupling the plating and stripping current density at different values, the performance can be optimized by balancing the macroscopic electrochemical observation and microscopic morphology during Li plating/stripping. This study provides new insights for further development of host structures and charge/discharge protocols for achieving the best LMA performance.

# 2. Materials and methods

# 2.1. Chemicals and materials

Electrolyte (1.0 M LiTFSI in DOL/DME (1:1, v/v) with 1 wt% LiNO $_3$  additive) was purchased from Dodochem Limited (Suzhou, China). Copper foils (99.999 %) were purchased from Fisher Scientific (Hampton, NH) and GoodFellow Corporation (Pittsburgh, PA). Li foil, CR2032 coin cell casings, spacers, and wave springs were purchased from MTI Corporation (Richmond, CA). Celgard 2400 separator was purchased from Celgard (Charlotte, NC).

# 2.2. Preparation of VACNF/Cu electrode

An  $84 \, \mu m$  thick copper foil was used as the substrate for the growth of VACNFs. A 300 nm thick Cr barrier layer and a 30 nm thick Ni catalyst layer were sputter coated using a high-vacuum Perkin Elmer 4400 series magnetron sputtering system at UHV Sputtering Inc. (Morgan Hill, CA). VACNFs were grown using a DC-biased PECVD unit (Black Magic, Aixtron, CA) following the same procedure reported in previous studies [27,39-42]. In brief, the substrate was heated to 500 °C at a rate of 200 °C/min with ammonia gas at a flow rate of 250 sccm, at a pressure of 3.9 Torr. Under these conditions, a DC plasma at 510 V and 40 W was applied for 60 s to dewet and break the Ni film into randomly distributed Ni nanoparticles. Then, the temperature was increased to 750 °C at a rate of 250 °C/min while 70 sccm acetylene gas was introduced as the carbon precursor along with ammonia, the etching/reducing gas, to give a steady-state pressure of 4.8 Torr. The process was continued for 90 min to grow  $\sim\!14~\mu m$  long VACNFs on Cu. For some experiments, we used VACNFs of  ${\sim}14~\mu m$  length, grown for 120 min on 100  $\mu m$  thick copper foil, with a 100 nm thick Cr barrier layer and a 24 nm thick Ni catalyst layer.

# 2.3. Materials characterization

The morphology of the electrodes was studied using Topcon/ISI/ABT

DS 130F FESEM (Akashi Beam Technology Corporation, Tokyo, Japan) and Helios NanoLab 660 (FEI, OR) with a focused ion beam (FIB) milling functionality. To image the electrodes after lithium plating/stripping, they were harvested from coin-cells by disassembling in an Ar-filled glovebox. The harvested electrodes were washed by immersing in DME several times. After drying in the antechamber of glovebox under vacuum, the FESEM samples were prepared back inside the glovebox. The prepared samples were then stored in a tightly sealed container filled with ultrapure Ar. The samples were only exposed to the ambient air for a few seconds during transfer from the sealed container to the sample stage of the FESEM. Before FIB milling, a 2  $\mu$ m thick Pt layer was deposited to protect the underneath structure from ion beam damage. The morphology of individual VACNFs was imaged using a Philips CM 100 TEM at a 100 kV acceleration voltage in the low dose mode at −175 °C using a Gatan cryo-holder. The VACNFs were transferred to TEM grids by scraping them from the electrode inside a glovebox. The TEM grids were stored in Ar-filled storage holders and plunged in liquid nitrogen without exposure to the air. This was followed by transferring the TEM grid to the cryo-holder using a cryo-station. The cryo-shield was used to prevent the sample from exposure to the air during the transfer from cryo-station to TEM.

# 2.4. Electrochemical characterization

VACNF/Cu or planar Cu foil electrodes of 15 mm in diameter were used as the working electrode to assemble half-cells using CR2032 casings. A 25  $\mu m$  thick Celgard 2400 and a 0.60 mm thick Li foil were used as the separator and counter electrode, respectively. A 0.3 mm thick stainless steel wave spring (1.4 mm height) and two pieces of 0.2 mm thick stainless-steel disk spacers were used as mechanical supports to provide consistent pressure and good contact between the components. Cell assembly was done using an MTI hydraulic crimping machine by applying  $\sim 750$  psi pressure. The Li foils were polished using 200 and 400 grit sandpapers before assembling. 250  $\mu L$  of 1.0 M LiTFSI in DOL/ DME (1:1, v/v) solvent with 1 wt% LiNO3 additive was used as the electrolyte. The half-cells were assembled in an argon-filled glovebox (Mbraun MB10 Compact, Stratham, NH) with oxygen and water levels below 0.5 ppm. To visualize the internal pressure inside coin cells, Fujifilm Prescale films (4LW, 3LW, 2LW, and LW) covering a range of pressures from 7.2 to 1400 psi were used in dry dummy cells with different compression % (see details in Fig. S2 and the following text descriptions in SI). The assembled half-cells were tested using a battery testing system (Neware, Shenzhen, China) at room temperature. Five cycles of Li intercalation/deintercalation at 50 µA were applied between 0.0 V and 1.0 V (vs. Li<sup>+</sup>/Li) before Li plating to activate the electrode. For the plating/stripping cycling tests, a capacity of 2.0 mAh/cm<sup>2</sup> was

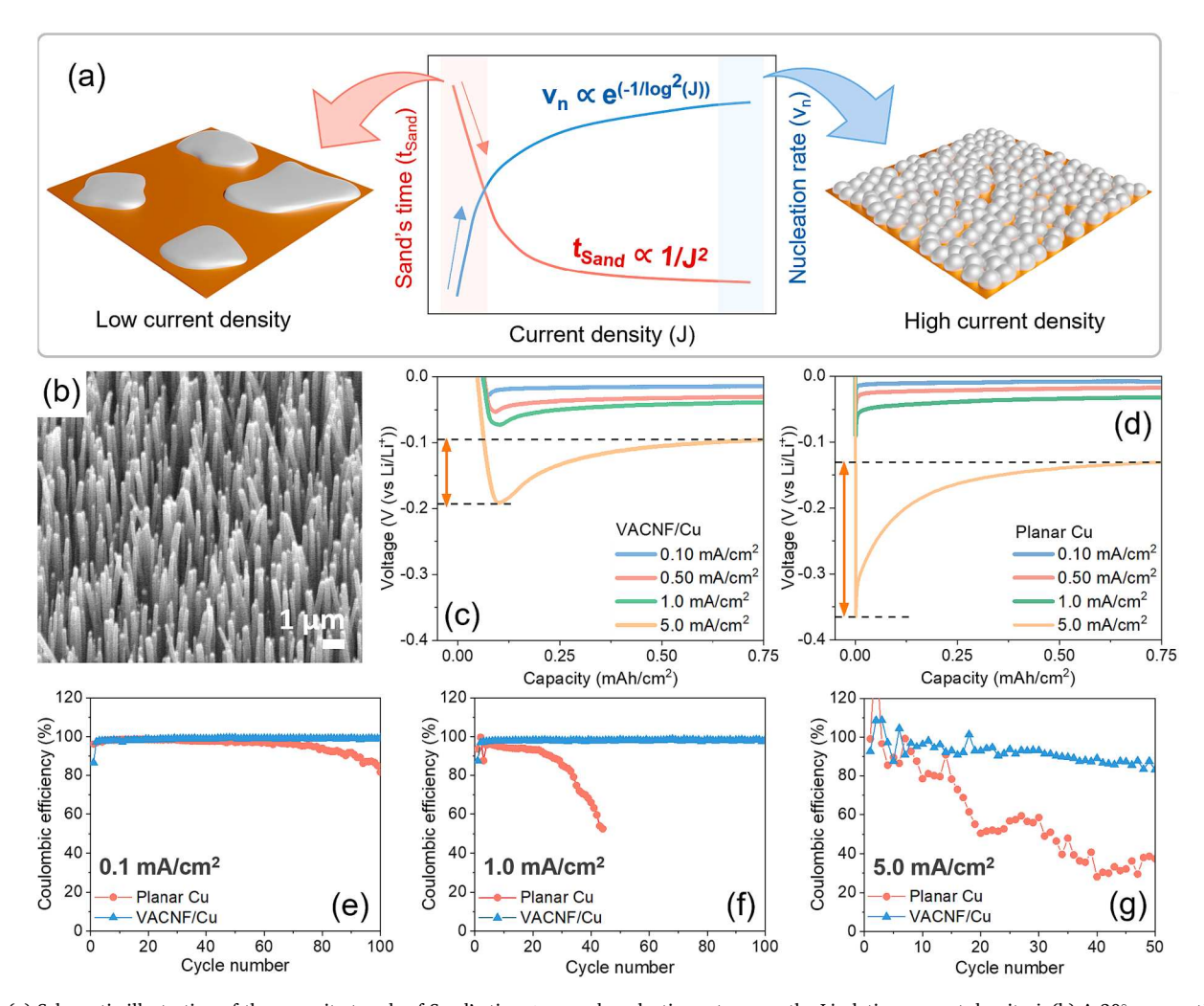


Fig. 1. (a) Schematic illustration of the opposite trends of Sand's time  $t_{Sand}$  and nucleation rate  $\nu_n$  vs. the Li plating current density j. (b) A 30° perspective view FESEM image of the pristine VACNF/Cu electrode. Li plating voltage curves at different current densities for (c) VACNF/Cu and (d) planar Cu electrodes. The coulombic efficiency during plating/stripping cycling of VACNF/Cu and planar Cu electrodes with a Li plating capacity of 2.0 mAh/cm<sup>2</sup> at the symmetric plating/stripping current density of (e) 0.10 mA/cm<sup>2</sup>, (f) 1.0 mA/cm<sup>2</sup>, and (g) 5.0 mA/cm<sup>2</sup>.

employed. The upper cut-off voltage for Li stripping was  $1.0~V~vs~Li^+/Li$ . The CE was determined by the ratio of the capacity of Li stripped to the capacity of Li plated, and it is expressed in percentage.

# 3. Results and discussion

#### 3.1. Preliminary characterization

Fig. 1a illustrates the opposite trends of Sand's time ( $t_{Sand}$ ) and nucleation rate ( $\nu_n$ ) vs. the plating current density j. Sand's time is defined as the time that it takes for the Li<sup>+</sup> ion concentration to deplete at the anode surface leading to the onset of ramified electric field and growth of dendrites. The relationship between  $t_{Sand}$  and the current density j is outlined in Equation 1 [43]:

$$t_{Sand} = \pi D_e \left( \frac{z_e C_0 F}{2j t_a} \right)^2 \tag{1}$$

where  $D_e$  is the effective diffusion coefficient,  $z_c$  is the charge of cation (+1 for Li<sup>+</sup> ion),  $C_0$  is the Li<sup>+</sup> concentration in the bulk electrolyte, and  $t_a$  is the anion transference number. Sand's time is inversely proportional to  $j^2$ . Thus, with the use of high-surface-area 3-D current collectors, the decrease in local current density helps to extend the Sand's time compared to planar electrodes and hence delay the onset of dendrite growth. However, the decrease in j also reduces the nucleation overpotential  $\eta_n$ , the driving force for Li nucleation and growth, leading to decrease in the nucleation rate  $\nu_n$  following Equation 2 [44]:

$$\nu_{\rm n} \propto \exp\left(-\frac{1}{\log^2 j}\right) \tag{2}$$

Associated with this, the nucleation density  $N_n$  also drastically decreases as j is reduced [14].

Based on literature, it is commonly accepted that the electrodeposition of lithium at low current densities leads to growth of large inhomogeneous islands without dendrite formation. While most studies in literature focused on the homogeneity of the electric field which is superior at low current densities, the impact of the nucleation rate  $\nu_n$  and nucleation density  $N_n$  are often overlooked [19]. The nucleation process is critical for lithium electrodeposition since it occurs rapidly within the short time at the beginning of electrodeposition and the further growth mainly occurs at the nucleated sites rather than forming fresh nuclei on the uncovered surface [45]. Given that 3-D current collectors inherently offer a lower local current density, it is expected that the nucleation density  $N_n$  will be further reduced, which will significantly affect the morphology of Li plating.

VACNF/Cu consists of a well-defined brush-like structure as shown in Fig. 1b. The TEM image (Fig. S1) of a representative VACNF shows the unique conically stacked graphitic cup structure under an inverse teardrop-shaped Ni nanoparticle catalyst at the tip. This unique structure provides abundant electrochemically active graphitic edges exposed on the sidewall surface. The structure and characteristics of VACNF/Cu electrode was thoroughly studied and documented in our previous reports [27,35,39-41]. The average diameter of the VACNFs used in this study was  $\sim 154$  nm and the length was controlled as  $\sim 14$  µm. Based on their high aspect ratio and density ( $\sim 1 \times 10^9$  fibers/cm<sup>2</sup>), it was estimated that the VACNF array provides ~ 70 times higher surface area than a planar current collector. The individual VACNFs were perpendicular to the copper substrate and were well separated from each other by about 100 - 300 nm, resulting in a low-tortuosity structure with a high porosity of  $\sim 79$  %. The VACNFs were found to be inherently doped with 7.3 at% of N across the whole CNF and 2.9 at% of O functionalized at the sidewall surface, which improved their lithiophilicity [27,35]. These properties are desired to enhance the performance as a conductive 3-D host for LMAs as demonstrated in our previous studies [27,35].

Fig. 1c and 1d show the typical galvanostatic voltage curves of the first Li plating step for VACNF/Cu and planar Cu electrodes,

respectively, at different current densities. For the planar Cu, a sharp voltage dip was observed during the electrodeposition, indicating the fast nucleation of Li without any intercalation/alloying. In the case of VACNF/Cu, the voltage dip was delayed to appear at the capacities of ~ 0.080 to 0.10 mAh/cm<sup>2</sup> due to partial Li intercalation into the graphitic structure of VACNFs, as reported in our previous studies [27,35]. With the increase in plating capacity, the voltage increased and formed a plateau with lower overpotentials, indicating reaching the steady-state Li growth limited by mass transport of Li<sup>+</sup> ions from the bulk solution. From these curves, lithium nucleation overpotentials  $(\eta_n)$  were calculated as the potential difference between the lowest voltage dip and the following plateau. The  $\eta_n$  was found to increase with the current density, consistent with Butler-Volmer kinetics. For VACNF/Cu, the  $\eta_{\text{n}}$  was observed to be 13.6, 23.0, 33.8 and 95.2 mV for the current density of 0.10, 0.50, 1.0 and 5.0 mA/cm<sup>2</sup>, respectively. Conversely, for planar Cu, the  $\eta_n$  was found to be 33.6, 44.3, 58.6 and 234.3 mV for the same respective current densities. It is evident that the magnitude of  $\eta_n$  was significantly smaller in 3-D VACNF/Cu than that of planar Cu electrode at all the tested current densities. This can be attributed to the lithiophilic nature and the high surface area of VACNF/Cu electrodes [35].

For further characterization, conventional symmetric plating/stripping cycling tests [46,47] were performed on VACNF/Cu and planar Cu electrodes at varied current densities (Fig. 1e-1g) with the plating and stripping current set at the same values. At the low current density with j = 0.10 mA/cm<sup>2</sup>, the cycling performance was relatively stable and lasted longer for both VACNF/Cu and planar Cu electrodes. VACNF/Cu exhibited a stable CE averaging around 98.8 % for 100 cycles, which is equivalent to 4000 h of cycling time. For the planar Cu, the CE declined to 81.5 % after 100 cycles. Under a higher cycling rate with j = 1.0 mA/cm<sup>2</sup>, the average CE slightly dropped to around 98.0 % for VACNF/Cu and the electrode was able to maintain a stable performance for 100 cycles. In comparison, the planar Cu failed quite early, with the CE dropped to 74.8 % after 35 cycles. With further increase in the current density to  $j = 5.0 \text{ mA/cm}^2$ , the performance of the planar Cu further degraded rapidly from the beginning of the cycling. The VACNF/Cu exhibited a better performance in comparison to the planar Cu, but its CE decreased from  $\sim 100$  % to  $\sim 83$  % after 50 cycles along with much larger variations in each cycle. The observed declining trend in CE and stability vs. the plating/stripping rate is consistent with other reports [48-50] and the prediction by the Sand's equation (Equation 1). From these results, it is concluded that the 3-D VACNF/Cu performs better than planar Cu at all cycling rates, which can be attributed to its 3-D conductive structure with superior lithiophilic nature to reduce Li dendrite formation. Here we focus on further study of the microscopic morphology of Li plating, which underlies the observed macroscopic performance enhancement in CE and cycle life [27,35].

# 3.2. Effect of plating/stripping kinetics on Li morphology

# 3.2.1. Effect on Li morphology by the internal pressure on the electrode surface

Our goal is to carry out morphological analysis to understand how the current density affects the structure of Li plating and its correlation on the cell performance. However, it is known that the morphology of electrodeposited Li strongly depends on the pressure inside the cells [9,51]. The discrepancies in morphology in literature are largely attributed to the uncontrolled pressure or non-uniform distribution of the pressure inside the cell [52,53]. Fig. S2 illustrates the internal configuration of the coin-cells used in this study. As revealed by the optical image of a pressure-sensitive film (Prescale film by Fujifilm) used in a dry dummy coin-cell, the pressure distribution inside the cell is highly nonuniform (Fig. 2a). A higher pressure was applied around the periphery than that at the center of the electrode disk. The morphological analysis of the electrode across its diameter was applied after plating 0.20 mAh/cm<sup>2</sup> of Li on the planar Cu disk at 0.10 mA/cm<sup>2</sup>. The SEM images revealed that the plated Li had distinct morphologies at

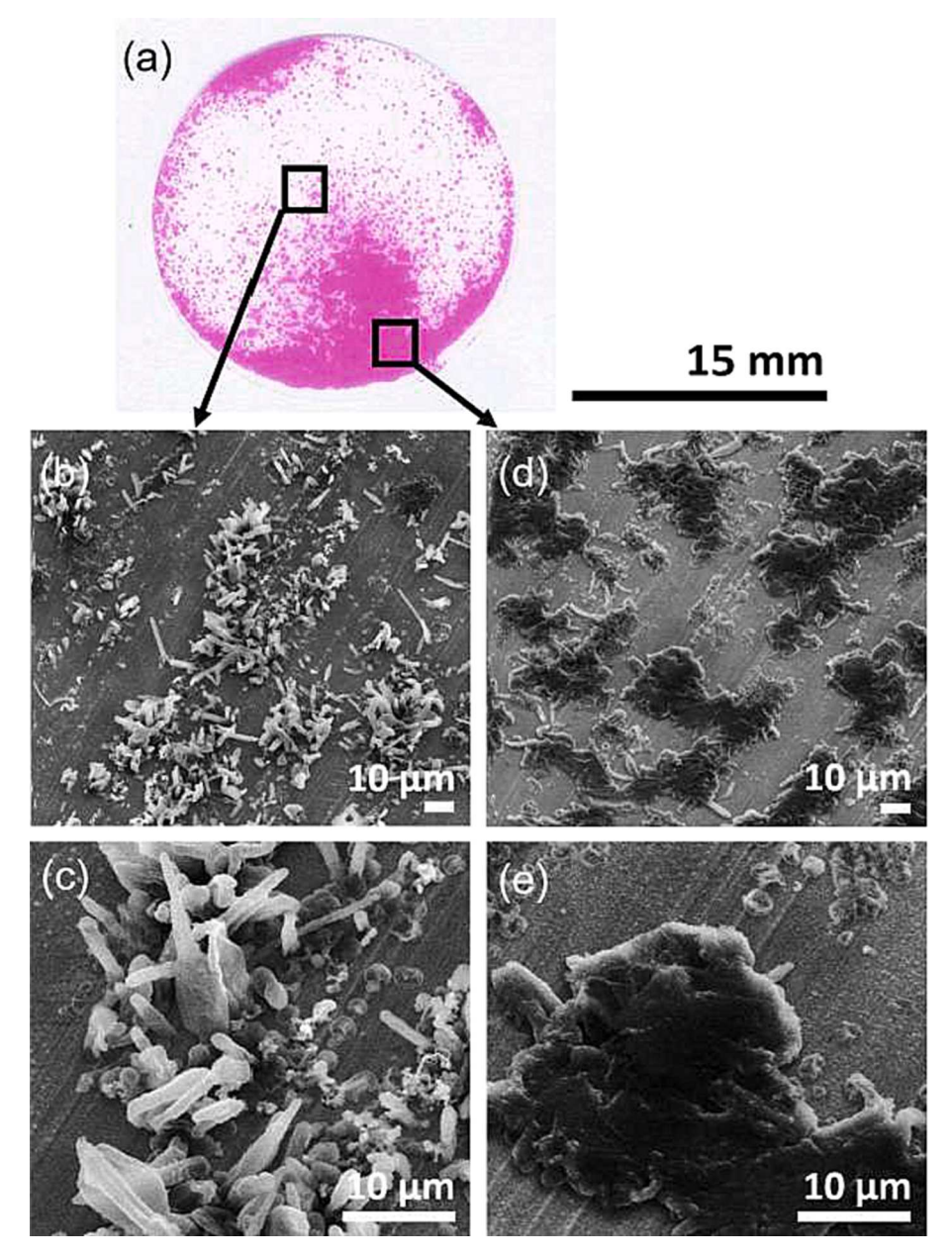


Fig. 2. (a) Optical image of a developed Prescale film showing the pressure distribution inside the coin cell configuration shown in Fig. S2. The 30° perspective view FESEM images of a planar Cu electrode plated with 0.20 mAh/cm² Li at 0.10 mA/cm² which are imaged at (b) & (c) center and (d) & (e) periphery of the electrode.

different locations. At the center of the electrode, the Li showed whisker or fibrous shapes (Fig. 2b and 2c) similar to the observation by Park et al. [31]. But at the spot close to the periphery, larger flat irregular Li islands were observed (Fig. 2d and 2e), consistent with the report by Pei et al. [14]. To further validate the pressure effect, studies were conducted by constructing coin-cells with increased internal pressure. Optical images of pressure-sensitive films with different internal pressures are shown in Fig. S3. With increase in compression% (as described in page S4 of the SI), the magnitude of internal pressure increases in both center and periphery but maintaining the non-uniform pressure distributions in coin-cells. The morphologies of Li plated at 0.10 mA/cm<sup>2</sup> up to 0.75 mAh/cm<sup>2</sup> capacity were examined at four different spots from the center to the edge of the planar Cu disk electrode. Fig. S4b - S4i were from a coin-cell with 16 % higher compression (see description in page S4 of the SI) which show a clear lateral expansion in the boundary of flat Li islands when moving from center to the edge. Interestingly, the compressed islands show darker contrast in SEM images, reflecting the dense and

more conductive Li metal grains while the uncompressed Li structures at the center show brighter features in SEM images. With further increase to 38 % higher compression, flat Li islands could be observed at all spots from the center to the edge of the electrode along with the presence of some fibrous Li at the island boundaries (Fig. S4j - S4q). The fraction of compressed flat Li islands increases when moving from the center to the edge. Clearly, the higher pressure causes formation of flat Li islands while the lower pressure leads to the intrinsic fibrous Li morphology. Such transformation from porous Li structures into dense compact structures under high pressures has also been observed in different electrolytes [37,51]. Our study confirmed the elastic deformation of Li deposits by pressure in the ether electrolyte that is commonly used for Li-S batteries. To exclude the pressure effect and examine the intrinsic morphology of Li plating, the following studies are carried out using the coin-cell configuration shown in Fig. S2 and focused on the spots at the center of the electrode which has the minimal internal pressure.

3.2.2. Effect on the morphology by Li plating/stripping kinetics on planar Cu

Fig. 3 shows the FESEM images of Li electrodeposited on planar Cu electrodes under different current densities (0.10, 1.0 and 5.0 mA/cm<sup>2</sup>) up to varied plating capacities (0.20, 0.75 and 2.0 mAh/cm<sup>2</sup>). As shown in Fig. 3a-3c, at the low current density of 0.10 mA/cm<sup>2</sup>, the plated Li mainly presents as long fiber-like structures (about 1.5 µm in diameter and 3 to 20 µm in length) mixed with a small number of Li spheres of 1.7  $\mu m$  in size (as highlighted by the blue arrows). Fig. S5a & S5b further show that the initial Li plating at the low capacity formed sparse nonuniformly distributed fibrous particles with Li nucleation clustered in some spots while a large portion of bare Cu surface is uncovered. As the plating capacity was increased, the diameter and length of fiber-like Li continued to increase while the size of Li spheres only increased slightly (Fig. S6). The inhomogeneous growth rate on the different Li nuclei is probably due to the inhomogeneous electric field at different Li structures. Close to the periphery of the electrode, instead of fiber-like Li, larger smooth island-like Li deposits were present due to higher pressure at the electrode surface (Fig. S7). Closer observation of these Li islands revealed that they consisted of individual Li fibers that merged into the large flat islands (Fig. S7). Some long fibers can be seen at the boundaries of the Li islands. Similar grain boundaries were observed by Pei et al. as well [14]. After completely stripping the 0.75 mAh/cm<sup>2</sup> of Li plated at 0.10 mA/cm<sup>2</sup> and 1.0 mA/cm<sup>2</sup>, respectively, clusters of dead Li

and SEI skins were observed (Fig. S8). Their scarce distribution is consistent with the low nucleation density at  $0.10~\text{mA/cm}^2$  plating current density.

When the plating current density was increased to  $1.0 \, \text{mA/cm}^2$ , the density of Li particles significantly increased, leaving a much smaller bare Cu surface area. The electrodeposited Li was dominated by spherical morphology ( $\sim 1.6 \, \mu \text{m}$  in diameter) with a smaller proportion of fiber-like Li (Fig. 3d–3f). Fig. S9 shows that the spherical Li particles stack to form multiple layers. When the capacity was increased to  $2.0 \, \text{mAh/cm}^2$ , further growth led Li particles to merge and form larger Li micro-columns ( $\sim 2.7 \, \mu \text{m}$  in diameter) (Fig. 3f). Upon completely stripping at the same current density ( $1.0 \, \text{mA/cm}^2$ ), dense dead Li/SEI structures with the irregular shapes of  $0.6 \, \text{to} \, 3.7 \, \mu \text{m}$  in size were left on the Cu surface (Fig. S10), consistent with the dense Li nucleation sites when it was plated at  $1.0 \, \text{mA/cm}^2$ .

A similar morphology of stacked spherical particles was observed when the current density was further increased to  $5.0~\text{mA/cm}^2$ . But the particle size was reduced to  $\sim 1.0~\text{\mu}\text{m}$  in diameter while the Cu surface was fully covered (Fig. 3g-3j). When they were stripped completely at  $5.0~\text{mA/cm}^2$ , a large amount of dead Li was observed as densely stacked spherical particles (Figs. S11a–S11c). At areas where they got stripped more effectively, crumbled SEI remnants with circular outlines were found. However, when the stripping current density was reduced to  $1.0~\text{mA/cm}^2$ , most spherical dead Li particles were removed

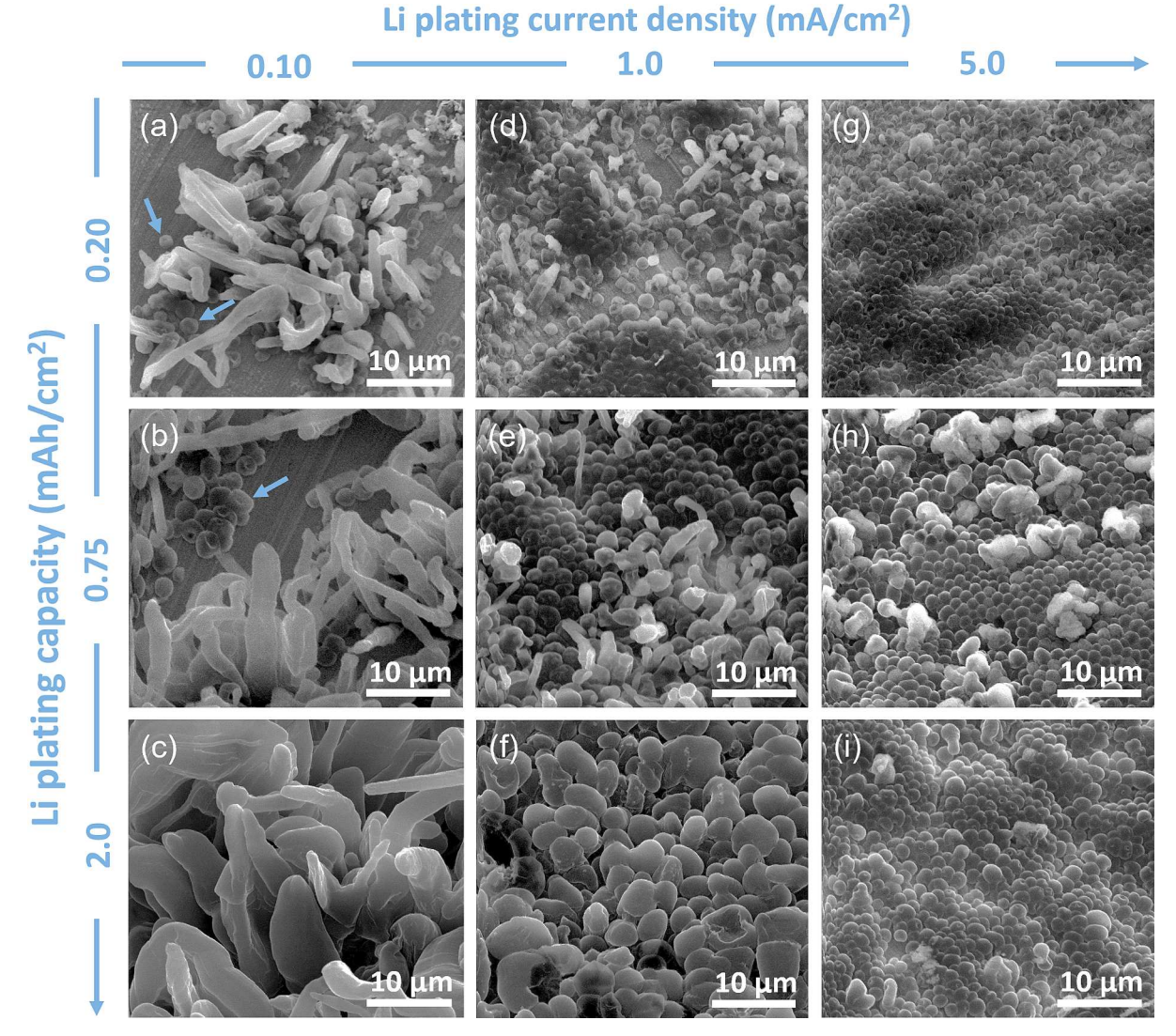


Fig. 3. The 30° perspective view FESEM images of electrodeposited Li on planar Cu electrodes at different current densities up to various plating capacities.

(Figs. S11d-S11f). Clearly, not only the plating current density but also the stripping current density is critical for the LMA performance. The application of a high stripping current density of 5.0 mA/cm<sup>2</sup> resulted in highly unstable cycling performance. It can thus be concluded that the inefficient stripping could be the cause for poor plating/stripping cycling performance of planar Cu at the high current density of 5.0 mA/ cm<sup>2</sup> (Fig. 1g) compared to those at the lower current densities (Fig. 1e and 1f). Similar findings were observed by other researchers as well [18]. However, contrary to common assumptions, among the tested conditions, the homogeneity in Li nucleation and growth is poor at the low current density of 0.10 mA/cm<sup>2</sup> [14,21,54,55]. Despite the heterogeneous growth, the use of low current density for the stripping step during CE cycling helps to achieve a relatively more stable performance, partially mitigated the impact of the electrodeposited lithium morphology. This illustrates that more attention should be given to microscopic nucleation kinetics in addition to the macroscopic battery tests.

# 3.2.3. Effect on the morphology by Li plating/stripping kinetics on 3-D VACNF/Cu

Fig. 4 shows the FESEM images of Li electrodeposited at different current densities on the 3-D VACNF/Cu electrodes. When electrodeposition was done at 0.10 mA/cm², sparsely distributed vertical Li microcolumns (or micropillars) of  $\sim 5.5~\mu m$  in diameter and height up

to  $\sim35~\mu m$  were observed even at a very low plating capacity of 0.20 mAh/cm² (Figs. 4a and S12a). An approximately equal number of darker recessed micro-spots were also observed in Fig. S12a, corresponding to the dense Li micro-grains infiltrated in the VACNF arrays. In the space between the bright protruding Li micro-columns and darker dense infiltrated micro-grains, the VACNF array is dominated by brush-like structure (Fig. S12b) similar to the pristine VACNF arrays (Fig. 1b). As described in our previous study [35], the fact that the VACNF array can maintain the vertical structure without collapsing into micro-bundles(or tipi-like structures) indicates that each VACNF is coaxially coated with nanoscale lithium or SEI sheaths which enhances its mechanical strength against the applied pressure in the coin-cell and the capillary forces exerted by the liquid electrolyte and the solvent during cell assembly/disassembly and rinsing processes. A detailed discussion on the coaxial Li/SEI coating is presented in a later section with TEM studies.

With further plating to 0.75 mAh/cm², the protruding microcolumns quickly grew in length, eventually folded along kinks into noodle-like structures on top of the VACNF array (Figs. 4b, S13a and S13b). Further growth was witnessed as the plating capacity was increased to 2.0 mAh/cm². The diameter of the Li fiber also increased to  $\sim 8.0 \ \mu m$  during this process but at a rate much slower than the increase in the length. On the periphery, due to higher internal pressure, dense Li islands were observed (Figs. S13c and S13d). As shown in Fig. S14, when completely stripped at 0.10 mA/cm², collapsed thin SEI skins from the

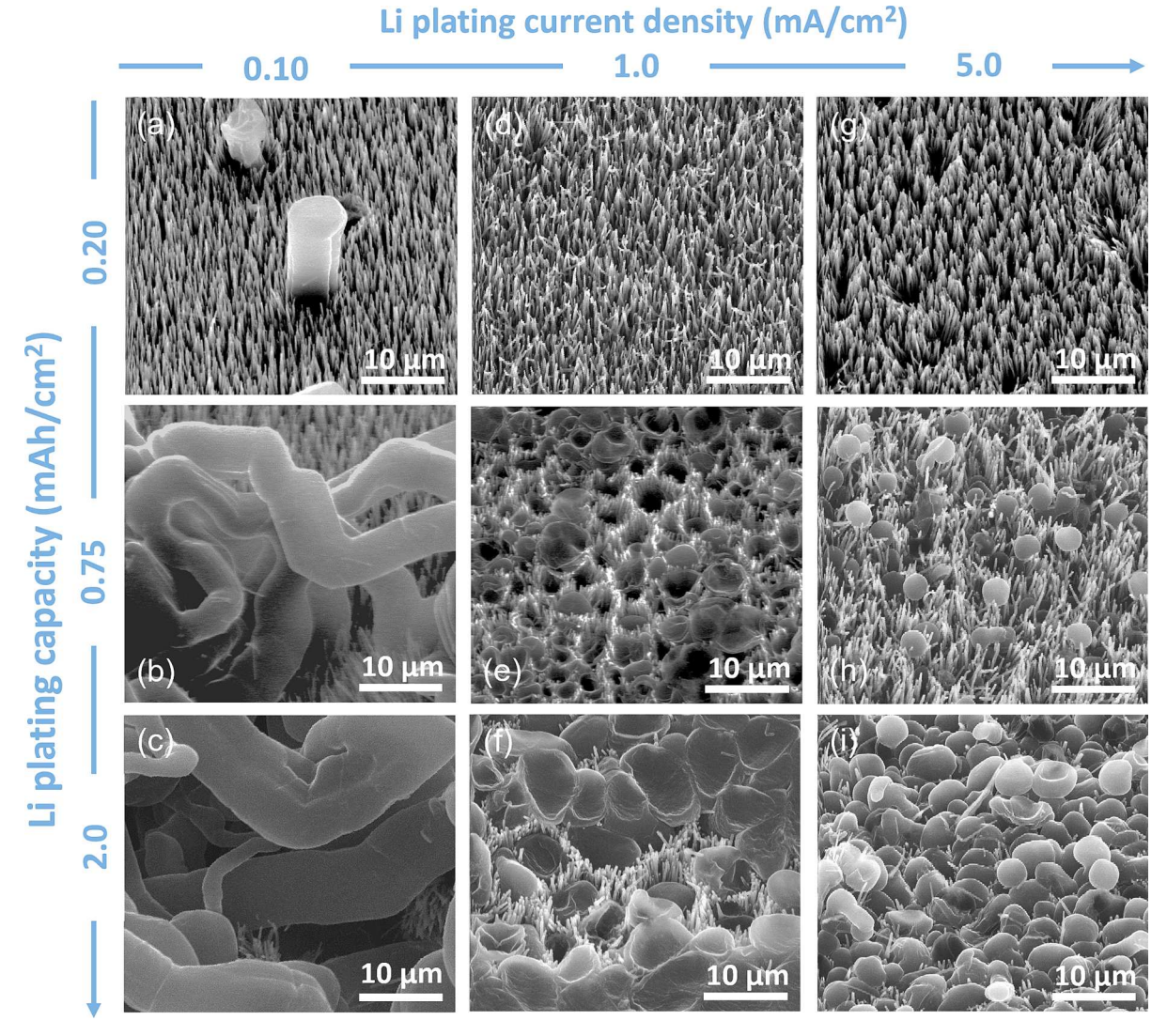


Fig. 4. The 30° perspective view FESEM images of electrodeposited Li on VACNF/Cu at different current densities up to various plating capacities.

surface of the noodle-like Li structure were left behind.

When the plating current density was increased to 1.0 mA/cm<sup>2</sup>, the growth of tall Li micro-columns was significantly suppressed (Fig. 4d). The plated Li at the low capacity (0.20 mAh/cm<sup>2</sup>) was dominated by coaxial Li sheath around each VACNFs (Figs. 4d and S12c). As the plating capacities was increased to 0.75 mAh/cm<sup>2</sup>, smaller (~3.0 to 4.9 um in diameter) and shorter Li micro-columns were formed inside the VACNF array (Fig. 4e). At the even higher plating capacity of 2.0 mAh/ cm<sup>2</sup>, the diameter of the Li micro-columns further increased and merged into larger solid columns of  $\sim$  4.8 to 10  $\mu m$  in diameter which encapsulated the VACNFs inside (Fig. 4f). The morphology change is consistent with the prediction by the classical theory of heterogeneous nucleation and growth, i.e., a higher nucleation rate  $\nu_n$  and a higher nucleation density  $N_n$  would be obtained at the higher plating current density (following the blue curve in Fig. 1b). It is to be noted that the height of Li micro-columns plated at  $i = 1.0 \text{ mA/cm}^2$  did not exceed ~  $20 \mu m$ . From the FIB-SEM image (Fig. S15), it can be observed that the columnar Li infiltrates the spaces among VACNFs to form dense solid structures without observable pores. Fig. S16 shows that no SEI skins were left on top of VACNF arrays after stripping the plated 0.75 mAh/ cm<sup>2</sup> Li. Instead, coaxial SEI sheaths were observed around the VACNFs that were buried within the Li micro-columns. Similar results were also observed at the plating current density of 0.50 mA/cm<sup>2</sup> (Fig. S17).

When the current density was increased further to 5.0 mA/cm<sup>2</sup>, small number of infiltrated Li micro-columns inside the VACNF array (Fig. 4g) and coaxial Li sheath (Fig. S12d) around individual VACNFs were observed at the low plating capacity of 0.20 mAh/cm<sup>2</sup>. As more Li is plated, in addition to the columnar Li infiltrated into the VACNF array, spherical Li particles of 2.4 to 3.2 µm in diameter were observed above the VACNF array and attached to the VACNF tips as shown in Fig. 4h-4i and \$18. This could signify the onset of more pronounced electric fields near the VACNF tips at high current densities [56], which might lead to rapid spherical Li deposition on top instead of infiltration into VACNF arrays. In the phase field modeling study by Xu et al., it was found that focused electric fields at the tips of pillar-like host structures at current densities  $\geq 5$  mA/cm<sup>2</sup> led to electrodeposition of lithium at their tips [57]. Similar electric field simulation studies in future could provide more insights into this phenomenon on VACNF arrays. The application of artificial SEIs along the length of VACNFs with a thickness gradient that decreases from the tip to the base could be an interesting strategy to explore in order to minimize the formation of spherical Li particles on VACNF tips. When stripped, the spherical Li particles disappeared but left behind crumbled SEI skins with circular borders (Fig. S19) similar to those observed on the planar Cu electrode. This implies that the spherical Li particles are electrically connected to the tip of VACNFs. In contrast to that on the planar Cu, patches of unstripped dead Li were not observed in VACNF/Cu even after stripping at 5.0 mA/cm<sup>2</sup>. This suggests an improved stripping efficiency of plated Li on VACNFs, probably due to the better electrical connectivity in the 3-D carbon host.

From Fig. 4, it can also be observed that some VACNFs were not engulfed by the infiltrated columnar Li in the samples. After plating with 0.75 mAh/cm² Li, these VACNFs were scraped off and analyzed using cryo-TEM (Fig. S20). It was found that, at all the tested current densities, there exists a co-axial sheath of electrodeposited Li on individual VACNFs. The thickness of the Li sheath ranges between  $\sim 20$  and  $\sim 110$  nm. After stripping, wrinkled SEI skins of 10-20 nm in thickness wrapping around the VACNFs can be observed (Fig. S21). The formation of such homogeneous coaxial Li sheath illustrates the lithiophilic nature of the graphitic edges of N- and O-doped VACNFs. The coaxial Li sheath formed quickly at the initial plating period up to about 0.20 mAh/cm² plating capacity at all plating current densities as shown in Figs. 4a, 4d, 4g, and S12b-S12d. However, the infiltrative columnar Li grew preferentially in the following plating period and thereby attributed to the dominant plated capacity.

# 3.2.4. Analysis of the Li grain size distributions

The size distribution of electrodeposited Li grains vs. the current density on VACNF/Cu and the planar Cu is depicted in Figs. 5a-5d and \$22, respectively. Only samples with a plating capacity of 0.75 mAh/ cm<sup>2</sup> were selected for the particle size analysis since the grains were well separated. At the plating current density  $j = 0.10 \text{ mA/cm}^2$ , the average size (i.e., the diameter of the fibrous structures) of electrodeposited Li on VACNF/Cu was 6.4 µm. With increase in current densities to 0.50, 1.0, and 5.0 mA/cm<sup>2</sup>, the average grain size was reduced to 4.0, 3.1, and 2.2 μm, respectively. In the case of planar Cu, the relationship between Li grain size and the current density j followed a similar trend with the average sizes of 2.8, 2.2, 1.9, and 1.5  $\mu$ m at j = 0.10, 0.50, 1.0, 5.0 mA/ cm<sup>2</sup>, respectively. The Li grain size on the VACNF/Cu host is significantly larger than that of planar Cu at all the tested current densities. This can be attributed to the lower local current density in VACNF/Cu host. The larger grain size, columnar morphology and improved electrical connectivity enabled by the VACNF/Cu host are beneficial in reducing undesired side reactions and boosting Li plating/stripping reversibility. This explains the enhanced stability in electrochemical cycling tests (Fig. 1e-1g). It needs to be highlighted that the distribution at  $0.10 \text{ mA/cm}^2$ , with a relative standard deviation (RSD) of  $\sim 44 \%$ , is much broader compared to that at higher current densities. This conveys a higher degree of heterogeneity at low current densities accompanied by the sparse nucleation.

For heterogeneous nucleation, the critical nuclei size ( $r_{crit}$ ) is inversely proportional to the nucleation overpotential  $\eta_n$  as given by Equation 3 [14]:

$$r_{crit} = \frac{2\gamma V_m}{F|\eta_n|} \tag{3}$$

where  $\Upsilon$  is the surface energy of Li-electrolyte interface,  $V_m$  is the molar volume of Li, and F is the Faraday's constant. The relationship between the current density j and the nucleation overpotential  $\eta_n$  is given by the Tafel equation, a special case of Butler-Volmer equation at low and moderate current densities:

$$\eta_n = A + B(\log j) \tag{4}$$

where A and B are constants. A linear relationship between  $\eta_n$  and  $\log j$  for j=0.10 to  $1.0~\mathrm{mA/cm^2}$  is indeed shown in Fig. 5e. At  $j=5.0~\mathrm{mA/cm^2}$ , deviation in the linear relationship was observed due to the change from kinetic-limited regime to mass-transfer limited regime. Clearly, the deviation observed on the planar Cu electrode is much larger than that on VACNF/Cu. Equations 3 and 4 predict that  $r_{crit}$  is inversely proportional to the  $\log j$ . Figs. 5f and S23 show the same trend, with the Li grain size ( $d_{Li}$ ) at 0.75 mAh/cm² plating capacity inversely proportional to  $\log j$  and  $\eta_n$ . This reveals that uniform Li nuclei can be obtained at proper plating current density. It is worth noting that the average Li grain size on VACNF/Cu deposited at 1.0 mA/cm² is larger than those deposited on Cu at a much lower current density of 0.10 mA/cm². This further validates the lower  $\eta_n$  offered by the 3-D VACNF/Cu electrode, which improves the Li plating/stripping reversibility compared to planar Cu electrode.

# 3.3. Optimal morphology for high performance

Based on the earlier discussion, the morphologies of electrodeposited Li on VACNF/Cu and planar Cu electrodes under the tested conditions are summarized in Fig. 6a. The overall process is highly heterogeneous and can be affected by both the structure of current collectors and the electrochemical deposition conditions, but it is consistent with the classical nucleation and growth theory. On planar Cu, at the low current density, the initial Li nucleation density is very low, but Li rapidly grows at these nucleation sites into large irregular grains consisting of clustered long fibers. With the increase in the current density, the nucleation density is increased, accompanied by the decrease in the nucleus size to

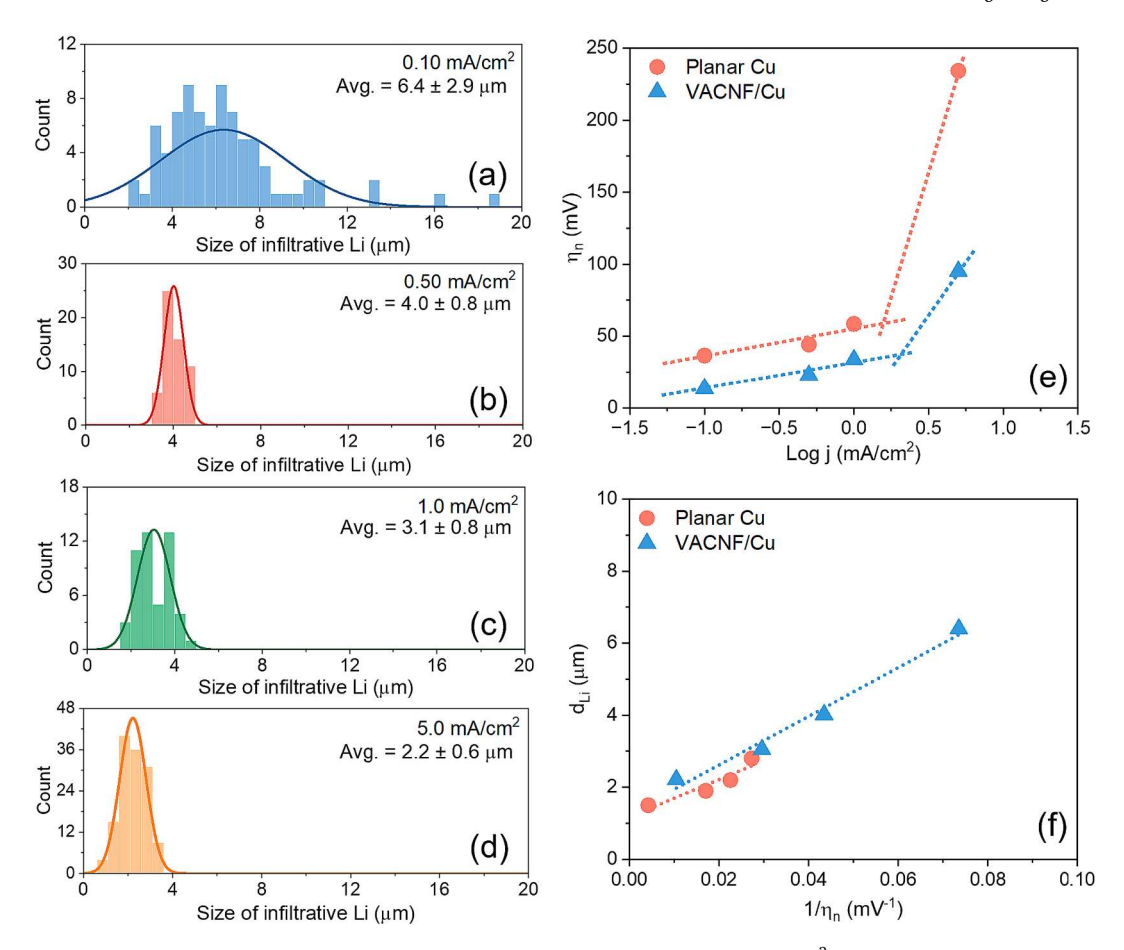


Fig. 5. Histogram of the size distribution of infiltrative Li grains electrodeposited to a capacity of 0.75 mAh/cm<sup>2</sup> on VACNF/Cu at current densities of (a) 0.10 mA/cm<sup>2</sup>, (b) 0.50 mA/cm<sup>2</sup>, (c) 1.0 mA/cm<sup>2</sup>, and (d) 5.0 mA/cm<sup>2</sup>. (e) The relationship between the Li nucleation overpotential ( $η_n$ ) and the plating current density (logj) for planar Cu and VACNF/Cu electrodes. (f) The correlation between the size of electrodeposited Li ( $d_{Li}$ ) and the inverse of Li nucleation overpotential ( $1/η_n$ ) on planar Cu and VACNF/Cu electrodes.

form uniformly distributed spherical particles (of a few microns in size) with presence of a small number of fiber-like structures. On the other hand, on the 3-D VACNF/Cu electrode, lithium is initially deposited as thin coaxial sheaths around each VACNFs at all plating current densities. When the plating capacity is larger than 0.10 mAh/cm<sup>2</sup> at a low current density ( $\leq 0.10 \text{ mA/cm}^2$ ), sparse columnar Li forms, which quickly grows into long fibers folded and laid over the VACNF array as more Li is plated. At the moderate plating current density (~1.0 mA/cm<sup>2</sup>), Li quickly forms columnar structure (a few microns in diameter) that infiltrates into the space among VACNFs. The micro-columns grow laterally and merge into larger grains that are mostly retained inside the VACNF array. When a high current density (5.0 mA/cm<sup>2</sup>) is applied, the density of columnar Li increases accompanied by a reduction in their diameter. In addition to the columnar Li, a significant amount of Li is deposited on the tip of VACNFs as spherical particles (with a unform diameter of a few microns).

In literature, the fiber- or noodle-like Li plated at low *j* is considered undesirable as it leads to porous deposition and inefficient stripping [33]. Contrary to this, such Li morphology exhibits higher CE and better stability during plating/stripping cycling (as shown in Fig. 1e). On the other hand, even though more unform Li particles infiltrated into VACNF arrays can be achieved at the high current density of 5.0 mA/cm², it exhibits poor cycling stability (as shown in Fig. 1g). The microscopic morphology and the macroscopic cycling tests seem to point the opposite directions for optimizing the performance. However, it is to be noted that the earlier cycling tests employed a symmetric protocol, i.e., having the identical current densities for Li plating and stripping processes. The stripping process at the low current density may not be an

issue but stripping at a high current density is known to produce a larger amount of dead Li [33], as shown in Figs. S11 and S19. Therefore, it is necessary to decouple the plating and stripping conditions to assess the stability of different Li morphologies. For this purpose, cycling tests were conducted on planar Cu and VACNF/Cu electrodes plated with 2.0 mAh/cm<sup>2</sup> Li using different plating current densities but stripped at a fixed moderate current density of 1.0 mA/cm<sup>2</sup>.

As shown in Fig. 6b, the cycling was stable for the VACNF/Cu electrodes plated at 1.0 and 5.0 mA/cm<sup>2</sup> which were associated with microcolumnar Li morphologies. The average CEs (from cycles 2-11) were around 97.8 % and 95.2 % for 1.0 and 5.0 mA/cm<sup>2</sup> plating current densities, respectively. The VACNF/Cu electrode at 0.10 mA/cm<sup>2</sup> plating current density exhibited the worst performance, with the CE starting to decline from the beginning of cycling and dropping below 80 % in the 15th cycle. After that, the CE started to increase and reached  $\sim$ 100 % after 40 cycles but with a large variation, possibly owing to the reconnection of accumulated dead Li [35]. The average CE (cycles 2-11) is only 88.1 %. This shows that the large noodle-like Li morphology may not exhibit a high cycling performance if the stripping current density is raised to a moderate level. In comparison, the cycling stability was inferior on planar Cu electrodes at all conditions (Fig. S24a) in similar decoupled plating/stripping studies. The planar Cu was unable to support the moderate stripping rate at 1.0 mA/cm<sup>2</sup> and was even worse at the stripping current density of 5.0 mA/cm<sup>2</sup> (Fig. S24b). Overall, as illustrated in Figs. S25 and S26, the micro-columnar Li morphology infiltrated in the VACNFs achieved at the moderate current density (j =1.0 mA/cm<sup>2</sup>) exhibited the highest performance with an average CE of  $\sim$  98 % (cycles 2–11). The Li spheres deposited on VACNF tips by the

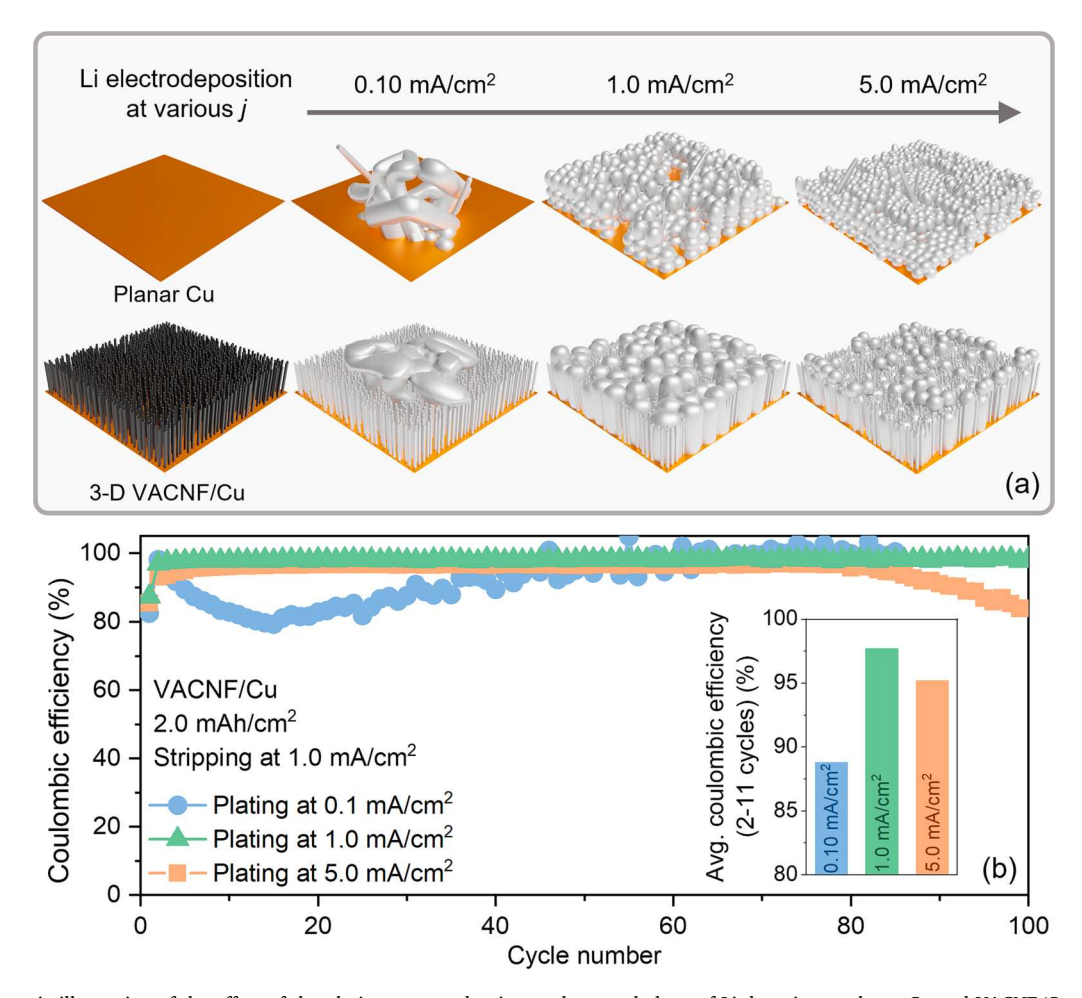


Fig. 6. (a) A schematic illustration of the effect of the plating current density on the morphology of Li deposits on planar Cu and VACNF/Cu electrodes. (b) The coulombic efficiency during plating/stripping cycling of 2.0 mAh/cm<sup>2</sup> Li plated on VACNF/Cu electrodes at different current densities but stripped at the fixed current density of 1.0 mA/cm<sup>2</sup>. Inset shows the average coulombic efficiency for cycles 2–11 at different plating current densities.

high current density ( $j=5.0~\text{mA/cm}^2$ ) gave a slightly lower CE ( $\sim$ 95%). The noodle-like Li morphologies plated at the low current density ( $j=0.10~\text{mA/cm}^2$ ) present the lowest CE ( $\sim$ 88%). This unveils that a lower plating current density is not always better for LMA operations, which is against the general presumption based on the Sand's equation (Equation 1). This provides an insight that factors other than lowering the local current density underlie the enhanced reversibility of Li plating/stripping on 3-D conductive anodes. To improve the nucleation density under low current densities and to induce dense Li structures, highly lithiophilic coatings could be applied to the host surface.

# 4. Conclusion

In summary, we have illustrated the correlation of the microscopic morphologies of electrodeposited lithium metal with the macroscopic performance in lithium plating/stripping cycling tests. The VACNF arrays were used as a model 3-D conductive carbon host with a well-defined vertically aligned low-tortuosity structure to compare with the planar Cu current collector. The 3-D VACNF host indeed provided much higher stability and reversibility for Li plating/stripping. The pressure on the electrode surface inside the coin-cells was found to significantly affect the morphology of Li plating, leading to discrepancies in literature. By excluding this factor, the intrinsic Li morphologies were studied at different plating current densities. It was found that Li plating on both VACNF array and planar Cu electrodes follows the classical nucleation and growth theory, with the nucleation density, nucleation rate, critical nucleation size and Li morphology regulated by the nucleation

overpotential which was proportional to the logarithm of the plating current density. At the low plating current density (≤0.10 mA/cm²), it tended to form sparse irregular grains of fibrous Li. At the moderate plating current density (~1.0 mA/cm<sup>2</sup>), it formed uniform smaller micro-columnar Li deposits. When a high plating current density (~5.0 mA/cm<sup>2</sup>) was used, some Li spheres started to form at the VACNF tips. In contrary to the Sand's equation which illustrates that a lower plating current density is always beneficial in suppressing Li dendrite formation, the morphology of Li deposits was more uniform at the moderate to high plating current densities, pointing to the opposite direction in optimizing lithium plating/stripping. We found that these seemingly contradictory trends were largely due to the neglected factor that stripping processes worked better at the lower current density. In conventional cycling tests, the stripping and plating current densities were set at the same values and thus lower plating/stripping current densities seemed to exhibit better cycling stability. By decoupling these two variables and fixing the stripping current density at  $\sim 1.0 \text{ mA/cm}^2$ , we unraveled that the Li metal deposit with more uniform microscopic morphology at the moderate plating current density ( $\sim 1.0 \text{ mA/cm}^2$ ) exhibited the highest performance. This provides new insights in optimizing the performance of LMAs based on 3-D conductive hosts. To extend the range of current densities that can induce favorable Li morphology, use of lithiophilic or artificial SEIs of gradient nature on 3-D hosts could be one of the promising strategies to study. Application of stable artificial SEIs would also prevent continuous formation and accumulation of dead Li and irreversible SEIs, which may further enhance the CE and cycle life.

# CRediT authorship contribution statement

**Sabari Rajendran:** Writing – original draft, Visualization, Validation, Methodology, Investigation, Formal analysis, Conceptualization. **Archana Sekar:** Writing – review & editing, Formal analysis. **Jun Li:** Writing – review & editing, Supervision, Resources, Project administration, Methodology, Funding acquisition, Formal analysis, Conceptualization.

# Declaration of competing interest

The authors declare that they have no known competing financial interests or personal relationships that could have appeared to influence the work reported in this paper.

# Data availability

Data will be made available on request.

# Acknowledgement

This work was partially supported by the US National Science Foundation grants CBET-2054754 and DMR-1707585. We would like to thank Dr. Dan Boyle at the Kansas State University Microscopy Facility in the Division of Biology for help in cryo-TEM imaging. The FIB-FESEM characterizations were performed in the Nebraska Nanoscale Facility: National Nanotechnology Coordinated Infrastructure and the Nebraska Center for Materials and Nanoscience (and/or NERCF), which are supported by the National Science Foundation under Award ECCS: 2025298 and the Nebraska Research Initiative.

# Appendix A. Supplementary data

Supplementary data to this article can be found online at https://doi.org/10.1016/j.cej.2024.149515.

# References

- N. Kittner, F. Lill, D.M. Kammen, Energy storage deployment and innovation for the clean energy transition, Nat Energy 2 (9) (2017) 1–6, https://doi.org/10.1038/ nenergy 2017 125
- [2] S. Kim, G. Park, S.J. Lee, S. Seo, K. Ryu, C.H. Kim, J.W. Choi, Lithium-metal batteries: from fundamental research to industrialization, Advanced Materials 35 (43) (2023) 2206625, https://doi.org/10.1002/adma.202206625.
- [3] J. Liu, Z. Bao, Y. Cui, E.J. Dufek, J.B. Goodenough, P. Khalifah, Q. Li, B.Y. Liaw, P. Liu, A. Manthiram, Y.S. Meng, V.R. Subramanian, M.F. Toney, V. V. Viswanathan, M.S. Whittingham, J. Xiao, W. Xu, J. Yang, X.-Q. Yang, J.-G. Zhang, Pathways for practical high-energy long-cycling lithium metal batteries, Nat Energy 4 (3) (2019) 180–186, https://doi.org/10.1038/s41560-019-0338-x.
- [4] S. Nanda, A. Gupta, A. Manthiram, Anode-free full cells: a pathway to high-energy density lithium-metal batteries, Advanced Energy Materials 11 (2) (2021) 2000804, https://doi.org/10.1002/aenm.202000804.
- [5] A. Shao, X. Tang, M. Zhang, M. Bai, Y. Ma, Challenges, strategies, and prospects of the anode-free lithium metal batteries, Advanced Energy and Sustainability Research 3 (4) (2022) 2100197, https://doi.org/10.1002/aesr.202100197.
- [6] B. Wu, C. Chen, L.H.J. Raijmakers, J. Liu, D.L. Danilov, R.-A. Eichel, P.H.L. Notten, Li-growth and SEI engineering for anode-free li-metal rechargeable batteries: a review of current advances, Energy Storage Materials 57 (2023) 508–539, https://doi.org/10.1016/j.ensm.2023.02.036.
- [7] R. Weber, M. Genovese, A.J. Louli, S. Hames, C. Martin, I.G. Hill, J.R. Dahn, Long cycle life and dendrite-free lithium morphology in anode-free lithium pouch cells enabled by a dual-salt liquid electrolyte, Nat Energy 4 (8) (2019) 683–689, https://doi.org/10.1038/s41560-019-0428-9.
- [8] F. Shi, A. Pei, A. Vailionis, J. Xie, B. Liu, J. Zhao, Y. Gong, Y. Cui, Strong texturing of lithium metal in batteries, Proceedings of the National Academy of Sciences 114 (46) (2017) 12138–12143, https://doi.org/10.1073/pnas.1708224114.
- [9] C. Fang, B. Lu, G. Pawar, M. Zhang, D. Cheng, S. Chen, M. Ceja, J.-M. Doux, H. Musrock, M. Cai, B. Liaw, Y.S. Meng, Pressure-tailored lithium deposition and dissolution in lithium metal batteries, Nat Energy 6 (10) (2021) 987–994, https:// doi.org/10.1038/s41560-021-00917-3.
- [10] Q. Zhao, Y. Deng, N.W. Utomo, J. Zheng, P. Biswal, J. Yin, L.A. Archer, On the crystallography and reversibility of lithium electrodeposits at ultrahigh capacity, Nat Commun 12 (1) (2021) 6034, https://doi.org/10.1038/s41467-021-26143-9.

- [11] X. Wang, G. Pawar, Y. Li, X. Ren, M. Zhang, B. Lu, A. Banerjee, P. Liu, E.J. Dufek, J.-G. Zhang, J. Xiao, J. Liu, Y.S. Meng, B. Liaw, Glassy li metal anode for high-performance rechargeable li batteries, Nat. Mater. 19 (12) (2020) 1339–1345, https://doi.org/10.1038/s41563-020-0729-1.
- [12] G. Zheng, S.W. Lee, Z. Liang, H.-W. Lee, K. Yan, H. Yao, H. Wang, W. Li, S. Chu, Y. Cui, Interconnected hollow carbon nanospheres for stable lithium metal anodes, Nature Nanotechnology 9 (8) (2014) 618–623, https://doi.org/10.1038/nnan/2014.152
- [13] K. Yan, J. Wang, S. Zhao, D. Zhou, B. Sun, Y. Cui, G. Wang, Temperature-dependent nucleation and growth of dendrite-free lithium metal anodes, Angewandte Chemie 131 (33) (2019) 11486–11490, https://doi.org/10.1002/ange.201905251.
- [14] A. Pei, G. Zheng, F. Shi, Y. Li, Y. Cui, Nanoscale nucleation and growth of electrodeposited lithium metal, Nano Lett 17 (2) (2017) 1132–1139, https://doi. org/10.1021/acs.nanolett.6b04755.
- [15] H. Sano, H. Sakaebe, H. Senoh, H. Matsumoto, Effect of current density on morphology of lithium electrodeposited in ionic liquid-based electrolytes, J. Electrochem. Soc. 161 (9) (2014) A1236, https://doi.org/10.1149/ 2.0331409jes.
- [16] H. Jung, B. Lee, M. Lengyel, R. Axelbaum, J. Yoo, Y.S. Kim, Y.S. Jun, Nanoscale detection of nucleation and growth of li electrodeposition at various current densities, Journal of Materials Chemistry A 6 (11) (2018) 4629–4635, https://doi.org/10.1039/c8ta00343b.
- [17] K. Dong, Y. Xu, J. Tan, M. Osenberg, F. Sun, Z. Kochovski, D.T. Pham, S. Mei, A. Hilger, E. Ryan, Y. Lu, J. Banhart, I. Manke, Unravelling the mechanism of lithium nucleation and growth and the interaction with the solid electrolyte Interface, ACS Energy Lett. 6 (5) (2021) 1719–1728, https://doi.org/10.1021/ acsenergylett.1c00551.
- [18] P. Biswal, S. Stalin, A. Kludze, S. Choudhury, L.A. Archer, Nucleation and early stage growth of li electrodeposits, Nano Lett. 19 (11) (2019) 8191–8200, https://doi.org/10.1021/acs.nanolett.9b03548.
- [19] X. Xu, X. Jiao, O.O. Kapitanova, J. Wang, V.S. Volkov, Y. Liu, S. Xiong, Diffusion limited current density: a watershed in electrodeposition of lithium metal anode, Advanced Energy Materials 12 (19) (2022) 2200244, https://doi.org/10.1002/ aenm.202200244.
- [20] Z.A. Ghazi, Z. Sun, C. Sun, F. Qi, B. An, F. Li, H.-M. Cheng, Key aspects of lithium metal anodes for lithium metal batteries, Small 15 (32) (2019) 1900687, https://doi.org/10.1002/smll.201900687.
- [21] D.T. Boyle, Y. Li, A. Pei, R.A. Vilá, Z. Zhang, P. Sayavong, M.S. Kim, W. Huang, H. Wang, Y. Liu, R. Xu, R. Sinclair, J. Qin, Z. Bao, Y. Cui, Resolving current-dependent regimes of electroplating mechanisms for fast charging lithium metal anodes, Nano Lett. 22 (20) (2022) 8224–8232, https://doi.org/10.1021/acs.nanolett.2c02792.
- [22] J.N. Chazalviel, Electrochemical aspects of the generation of ramified metallic electrodeposits, Phys. Rev. A 42 (12) (1990) 7355–7367, https://doi.org/10.1103/ PhysRevA.42.7355.
- [23] D. Aurbach, E. Zinigrad, Y. Cohen, H. Teller, A short review of failure mechanisms of lithium metal and lithiated graphite anodes in liquid electrolyte solutions, Solid State Ionics 148 (3) (2002) 405–416, https://doi.org/10.1016/S0167-2738(02) 00080-2
- [24] K.N. Wood, E. Kazyak, A.F. Chadwick, K.-H. Chen, J.-G. Zhang, K. Thornton, N. P. Dasgupta, Dendrites and pits: untangling the complex behavior of lithium metal anodes through operando video microscopy, ACS Cent. Sci. 2 (11) (2016) 790–801, https://doi.org/10.1021/acscentsci.6b00260.
- [25] D. Lin, Y. Liu, Y. Cui, Reviving the lithium metal anode for high-energy batteries, Nature Nanotechnology 12 (3) (2017) 194–206, https://doi.org/10.1038/ nnano 2017 16
- [26] J. Lang, L. Qi, Y. Luo, H. Wu, High performance lithium metal anode: Progress and prospects, Energy Storage Materials 7 (2017) 115–129, https://doi.org/10.1016/j. ensm.2017.01.006.
- [27] Y. Chen, A. Elangovan, D. Zeng, Y. Zhang, H. Ke, J. Li, Y. Sun, H. Cheng, Vertically aligned carbon nanofibers on cu foil as a 3D current collector for reversible li plating/stripping toward high-performance Li–S batteries, Advanced Functional Materials 30 (4) (2020) 1906444, https://doi.org/10.1002/adfm.201906444.
- [28] C.-P. Yang, Y.-X. Yin, S.-F. Zhang, N.-W. Li, Y.-G. Guo, Accommodating lithium into 3D current collectors with a submicron skeleton towards long-life lithium metal anodes, Nat Commun 6 (1) (2015) 8058, https://doi.org/10.1038/ncomms9058.
- [29] X. Fan, Y. Li, C. Luo, S. Luo, B. Huang, S. Liu, W. Sun, Vertically aligned MnO2 nanosheets on carbon fiber cloth as lithiophilic host enables dendrite-free lithium metal anode, Electrochimica Acta 464 (2023) 142896, https://doi.org/10.1016/j.electacta.2023.142896.
- [30] Y. Wang, H.-Q. Sang, W. Zhang, Y. Qi, R.-X. He, B. Chen, W. Sun, X.-Z. Zhao, D. Fu, Y. Liu, Electrophoretic deposited black phosphorus on 3D porous current collectors to regulate li nucleation for dendrite-free lithium metal anodes, ACS Appl. Mater. Interfaces 12 (46) (2020) 51563–51572, https://doi.org/10.1021/acsami.0c16430.
- [31] S.H. Park, Y.J. Lee, Morphological control of electrodeposited lithium metal via seeded growth: stepwise spherical to fibrous lithium growth, Journal of Materials Chemistry A 9 (3) (2021) 1803–1811, https://doi.org/10.1039/D0TA10006D.
- [32] Z. Huang, G. Zhou, W. Lv, Y. Deng, Y. Zhang, C. Zhang, F. Kang, Q.-H. Yang, Seeding lithium seeds towards uniform lithium deposition for stable lithium metal anodes, Nano Energy 61 (2019) 47–53, https://doi.org/10.1016/j. nanoen.2019.04.036.
- [33] C. Fang, J. Li, M. Zhang, Y. Zhang, F. Yang, J.Z. Lee, M.-H. Lee, J. Alvarado, M. A. Schroeder, Y. Yang, B. Lu, N. Williams, M. Ceja, L. Yang, M. Cai, J. Gu, K. Xu, X. Wang, Y.S. Meng, Quantifying inactive lithium in lithium metal batteries, Nature 572 (7770) (2019) 511–515, https://doi.org/10.1038/s41586-019-1481-z.

- [34] J. Li, G.P. Pandey, Advanced physical chemistry of carbon nanotubes, Annual Review of Physical Chemistry 66 (1) (2015) 331–356, https://doi.org/10.1146/ annurev-physchem-040214-121535.
- [35] S. Rajendran, A. Sekar, J. Li, Mechanistic understanding of li metal anode processes in a model 3D conductive host based on vertically aligned carbon nanofibers, Carbon 212 (2023) 118174, https://doi.org/10.1016/j.carbon.2023.118174.
- [36] Y. He, X. Ren, Y. Xu, M.H. Engelhard, X. Li, J. Xiao, J. Liu, J.-G. Zhang, W. Xu, C. Wang, Origin of lithium whisker formation and growth under stress, Nature Nanotechnology 14 (11) (2019) 1042–1047, https://doi.org/10.1038/s41565-019-0558-z.
- [37] E. Kazyak, M.J. Wang, K. Lee, S. Yadavalli, A.J. Sanchez, M.D. Thouless, J. Sakamoto, N.P. Dasgupta, Understanding the electro-chemo-mechanics of li plating in anode-free solid-state batteries with operando 3D microscopy, Matter 5 (11) (2022) 3912–3934, https://doi.org/10.1016/j.matt.2022.07.020.
- [38] X. Shen, R. Zhang, P. Shi, X. Chen, Q. Zhang, How does external pressure shape li dendrites in li metal batteries? Advanced Energy Materials 11 (10) (2021) 2003416, https://doi.org/10.1002/aenm.202003416.
- [39] S.A. Klankowski, R.A. Rojeski, B.A. Cruden, J. Liu, J. Wu, J. Li, A high-performance lithium-ion battery anode based on the core-shell heterostructure of silicon-coated vertically aligned carbon nanofibers, Journal of Materials Chemistry A 1 (4) (2013) 1055–1064, https://doi.org/10.1039/C2TA00057A.
- [40] J. Liu, J. Essner, J. Li, Hybrid supercapacitor based on coaxially coated manganese oxide on vertically aligned carbon nanofiber arrays, Chem. Mater. 22 (17) (2010) 5022–5030, https://doi.org/10.1021/cm101591p.
- [41] S.S.H. Zaidi, S. Rajendran, A. Sekar, A. Elangovan, J. Li, X. Li, Binder-free li-O<sub>2 (/sub> battery cathodes using ni- and PtRu-coated vertically aligned carbon nanofibers as electrocatalysts for enhanced stability, Nano Research Energy 2 (2) (2023) e9120055. https://doi.org/10.26599/NRE.2023.9120055.
- [42] S.A. Klankowski, G.P. Pandey, B.A. Cruden, J. Liu, J. Wu, R.A. Rojeski, J. Li, Anomalous capacity increase at high-rates in lithium-ion battery anodes based on silicon-coated vertically aligned carbon nanofibers, Journal of Power Sources 276 (2015) 73–79, https://doi.org/10.1016/j.jpowsour.2014.11.094.
- [43] C. Brissot, M. Rosso, J.N. Chazalviel, S. Lascaud, Dendritic growth mechanisms in lithium/polymer cells, Journal of Power Sources 81–82 (1999) 925–929, https:// doi.org/10.1016/S0378-7753(98)00242-0.
- [44] Z. Hou, Y. Gao, R. Zhou, B. Zhang, Unraveling the rate-dependent stability of metal anodes and its implication in designing cycling protocol, Advanced Functional Materials 32 (7) (2022) 2107584, https://doi.org/10.1002/adfm.202107584.
- [45] G. Feng, Y. Shi, H. Jia, S. Risal, X. Yang, P. Ruchhoeft, W.-C. Shih, Z. Fan, W. Xu, X. Shan, Progressive and instantaneous nature of lithium nucleation discovered by dynamic and operando imaging, science, Advances 9 (21) (2023) eadg6813, https://doi.org/10.1126/sciadv.ade6813.
- [46] B.D. Adams, J. Zheng, X. Ren, W. Xu, J.-G. Zhang, Accurate determination of coulombic efficiency for lithium metal anodes and lithium metal batteries,

- Advanced Energy Materials 8 (7) (2018) 1702097, https://doi.org/10.1002/
- [47] A. Mohammadi, S. Djafer, S. Sayegh, A.J. Naylor, M. Bechelany, R. Younesi, L. Monconduit, L. Stievano, Assessing coulombic efficiency in lithium metal anodes, Chem. Mater. 35 (6) (2023) 2381–2393, https://doi.org/10.1021/acs. chemmater.2c03518.
- [48] S. Wang, J. Qu, F. Wu, K. Yan, C. Zhang, Cycling performance and kinetic mechanism analysis of a li metal anode in series-concentrated ether electrolytes, ACS Appl. Mater. Interfaces 12 (7) (2020) 8366–8375, https://doi.org/10.1021/ acsami.9b23251.
- [49] J.-D. Xie, W.-J. Liu, C. Li, J. Patra, Y.A. Gandomi, Q.-F. Dong, J.-K. Chang, Superior coulombic efficiency of lithium anodes for rechargeable batteries utilizing highconcentration ether electrolytes, Electrochimica Acta 319 (2019) 625–633, https://doi.org/10.1016/j.electacta.2019.07.020.
- [50] X. Liu, P. Xu, J. Zhang, X. Hu, Q. Hou, X. Lin, M. Zheng, Q. Dong, A highly reversible lithium metal anode by constructing lithiophilic bi-nanosheets, Small 17 (45) (2021) 2102016, https://doi.org/10.1002/smll.202102016.
- [51] W. Deng, X. Yin, W. Bao, X. Zhou, Z. Hu, B. He, B. Qiu, Y.S. Meng, Z. Liu, Quantification of reversible and irreversible lithium in practical lithium-metal batteries, Nat Energy 7 (11) (2022) 1031–1041, https://doi.org/10.1038/s41560-023-0130-8
- [52] Z. Yu, P.E. Rudnicki, Z. Zhang, Z. Huang, H. Celik, S.T. Oyakhire, Y. Chen, X. Kong, S.C. Kim, X. Xiao, H. Wang, Y. Zheng, G.A. Kamat, M.S. Kim, S.F. Bent, J. Qin, Y. Cui, Z. Bao, Rational solvent molecule tuning for high-performance lithium metal battery electrolytes, Nat Energy 7 (1) (2022) 94–106, https://doi.org/10.1038/s41560-021-00962-v.
- [53] X.D. Ren, L.F. Zou, X. Cao, M.H. Engelhard, W. Liu, S.D. Burton, H. Lee, C.J. Niu, B. E. Matthews, Z.H. Zhu, C.M. Wang, B.W. Arey, J. Xiao, J. Liu, J.G. Zhang, W. Xu, Enabling high-voltage lithium-metal batteries under practical conditions, Joule 3 (7) (2019) 1662–1676, https://doi.org/10.1016/j.joule.2019.05.006.
- [54] J. Jeon, G.H. Yoon, T. Vegge, J.H. Chang, Phase-field investigation of lithium electrodeposition at different applied overpotentials and operating temperatures, ACS Appl. Mater. Interfaces 14 (13) (2022) 15275–15286, https://doi.org/ 10.1021/acsami.2c00900.
- [55] X. Sun, X. Zhang, Q. Ma, X. Guan, W. Wang, J. Luo, Revisiting the electroplating process for lithium-metal anodes for lithium-metal batteries, Angewandte Chemie International Edition 59 (17) (2020) 6665–6674, https://doi.org/10.1002/ anie.201912217.
- [56] J. Chen, X. Qiao, W. Fu, X. Han, Q. Wu, Y. Wang, Y. Zhang, L. Shi, J. Zhao, Y. Ma, Lithiophilic hyperbranched cu nanostructure for stable li metal anodes, SmartMat 4 (3) (2023) e1174. https://doi.org/10.1002/smm2.1174.
- [57] X. Xu, Y. Liu, J.-Y. Hwang, O.O. Kapitanova, Z. Song, Y.-K. Sun, A. Matic, S. Xiong, Role of li-ion depletion on electrode surface: underlying mechanism for electrodeposition behavior of lithium metal anode, Advanced Energy Materials 10 (44) (2020) 2002390, https://doi.org/10.1002/aenm.202002390.